The International Journal of Advanced Manufacturing Technology (2018) 96:4123–4143
https://doi.org/10.1007/s00170-018-1840-1

ORIGINAL ARTICLE

A numerical investigation for alternative toolpath deposition solutions for surface cladding of stainless steel P420 powder on AISI 1018 steel substrate

Navid Nazemi[1] · Ruth Jill Urbanic[1]

Received: 22 September 2017 / Accepted: 26 February 2018 / Published online: 19 March 2018

Abstract
The thermal cycling in the coaxial laser cladding process can cause significant variations in the strength of cladded parts as well as the development of residual stresses, large distortions, and even cracking. In the current study, the hardness variations, induced residual stress distribution, and the developed distortion characteristics of cladded parts are examined for different deposition tool paths. The research is conducted by means of numerical simulations validated by experimental results for selected surface cladding deposition strategies. The specimens were made using P420 stainless steel powder clad onto an AISI 1918 substrate. In the previous studies by the authors, it was found that the transient thermal solution using a moving heat source simulation technique required several days of computational time for small cladded parts, making it impractical for industrial applications. In the present research work, a modeling approach using a steady-state thermal solution was proposed. This technique produced similar results for hardness and residual stress in a shorter time period, but the resulted distortion values were not accurate. Consequently, a thermo-mechanical modeling approach was adopted that provided virtual distortion solutions correlating well with the experimental results. These models were subsequently employed to explore various process planning scenarios. The effect of surface cladding deposition patterns, the substrate dimensions, the plate dimension's aspect ratio, and the time gap between beads deposition were simulated and the strength and physical defects of the clad layer results are compared. Moreover, the mechanical response and properties for a full-scale gasket part is investigated as an example representing an industrial application.

Keywords Finite element modeling · Laser cladding · Residual stress · Distortion · Steel

1 Introduction

Many industries, such as the aerospace and automotive industries, employ coaxial laser cladding with powder feeding as a surface treatment technique to enhance the mechanical properties of the surface of a metallic substrate by depositing a material with superior corrosion and wear resistance. In addition, laser cladding is being adopted for repair or geometrical dimension restoration purposes, and as an additive manufacturing (AM) technique. However, the inherent drawback with the laser cladding process is the negative effect of the high temperature cycles on the strength and plastic properties of the cladded components, which induces residual stresses and distortions. High residual stress peaks caused by depositing multi-beads may be detrimental to fatigue performance as they can contribute to high mean stress effects under axial tensile cyclic loading. Distortion negatively impacts the dimensional accuracy, which in turn may influence the mechanical performance of parts. These effects can be neutralized to some extent by using thermal and nonthermal techniques. Thermal treatment approaches such as pre- and post-heat treatment [1, 2] are used to counterbalance the unwanted residual stress. Mechanical treatment procedures include stress relief techniques such as vibratory stress relief and shot peening [3], geometrical dimension restoration techniques including subtractive

✉ Navid Nazemi
nazemi@uwindsor.ca

Ruth Jill Urbanic
jurbanic@uwindsor.ca

[1] Department of Mechanical, Automotive, & Materials Engineering, University of Windsor, Windsor, ON N9B 3P4, Canada

processes, and finishing operations such as high-speed machining [4]. However, these processes increase the time and cost of the manufacturing. Therefore, it is a priority to achieve cladded parts with high and uniform strength and with minimal physical defects by optimizing the process parameters, as well as the deposition pattern.

Many researchers have employed numerical modeling approaches to simulate laser cladding using a transient thermal solution as a reliable and practical tool to study the mechanical response of cladded parts. Published work includes studies on single clad bead deposition models ([5–9]) and multi-track bead deposition models for surface cladding [10–16], as well as multiple clad beads for stacking or layering to form a wall structure ([4, 17–19], Zhang et al. [20], Alimardani et al. [21]) with applications in rapid prototyping and repair in industries such as automotive and aerospace.

Santhanakrishnan et al. [8] focused on predicting the hardening effects of laser cladding. The acquired temperature history from the finite element (FE) model was used to predict the temperature gradient, rates of heating and cooling cycles, and solidification of the clad to the substrate using various boundary conditions, laser power, and scanning speed. The thermal model results were coupled with thermo-kinetic equations to predict the hardness of the clad and substrate. Their investigation on the microstructure showed that four different zones exist with fine to coarse dendrite and cellular structure across the clad. Alimardani et al. (2007) proposed a method for predicting thermal cycles and geometrical characteristics of multi-layered cladding deposition depending on material properties and cladding process parameters. They developed a geometry build-up simulation approach in a discretized step-wise method. Their results indicated that the endpoint of deposited layers except the first layer was notably thicker and the temperature was higher due to the changes in the heat transfer mechanism. Moreover, they concluded that the pick-up efficiency of powder in the first layer is significantly lower than the subsequent layers.

Zhang et al. (2011) developed a thermo-mechanical model to simulate the multi-bead pulsed laser powder deposition process applied to the Ni-based turbine blade repair. The correlation of the temperature gradient and von Mises stress gave an insight into the critical value range and location in the deposit, in which the formation of stray grains and cracks is most likely to occur. Salonitis et al. [4] presented a methodology to simulate the successive deposition of laser cladding beads as an additive manufacturing process followed by high-speed machining. They employed the level-set method to define the cutting tool path to predict residual stresses and distortion results in a steel tube fabricated by laser cladding. Their results show that removal of a small amount of material relaxes residual stresses in the parts of the tube not constrained by the base plate and partially eliminates the distortion caused by laser cladding.

Chew et al. [10] developed a sequentially coupled thermo-mechanical model to predict the induced residual stress due to coaxial powder laser cladding of AISI 4340 steel powder onto a similar substrate material with various deposition scenarios. They proposed a model for laser power attenuation and powder concentration distribution for the laser-powder-interaction zone under the feeding nozzle. Their study showed that for a single bead specimen, across the substrate surface, the model predicted high tensile longitudinal and transverse stress values near the center and compressive further away. The reheating due to deposition of the second clad bead and subsequent laser heat pass was found to reduce the longitudinal tensile residual stresses caused by previous clad beads.

Zhang et al. [9] developed a model to study the thermal results such as the temperature gradient and solidification rate during laser cladding of 420 stainless steel + 4% molybdenum onto a mild steel (A36) substrate. In their model, the effects of laser-powder interaction, temperature-dependent material properties, latent heat, and Marangoni flow were considered. Based on the simulated thermal results, they studied the microstructure and molybdenum distribution in the clad layer. Gouge et al. [12] developed a model to implement thermal convection into the FE analysis of laser cladding. They compared two common convection implementations of no convection and free convection with three forced convection methods. It was shown that the convection model must be applied to an evolving surface to capture the change of part geometry due to the addition of material during the cladding process.

Based on the mentioned literature, FE analysis (FEA) is commonly used to help to understand and improve the quality of the process, and lowers the cost and time spent on conducting physical experiments. FEA has been proven to be a powerful numerical tool which can be used to predict the structural performance of components produced by AM processes. This technique has been employed to optimize the mechanical and physical properties (strength, residual stress, and distortion) by adjusting the process parameters, as well as deposition pattern and configuration accordingly. Therefore, the AM industry can benefit from this simulation technique in the product and process development phases. However, the major obstacle appearing when it comes to the exploitation of FEA by industry is the high computational cost. The conventional transient models are not efficient for simulating a large-scale manufacturing process. From an industrial perspective, the computation running time for the simulation is relatively high due to the transient nature of the analysis that prevents the application of FEA for on-line process optimization. Therefore, emphasis should be given to intelligent approaches to reduce the modeling complexity without sacrificing accuracy. The simplest and most popular approach is applying a coarser mesh as moving away from the heat source and lowering the total number of elements. However, there is a limit how much the element size can be increased while not losing its accuracy and convergence.

Another strategy is replacing the Moving Heat Source with a heat flux applied simultaneously to the whole area of each deposition layer, which can be defined as an instantaneous heat source [22–24]. The computational effort can be reduced significantly by using a steady-state analysis instead of a transient that decreases the number of time steps to one. Pu et al. [24] developed three different modeling approaches and compared their prediction accuracy and computation time: (i) a model with moving heat source, (ii) a model with instantaneous heat source, and (iii) a model with instantaneous heat source as well as coarser mesh density. They investigated welding residual stress and distortion in a low-alloy high-strength Q345 steel multi-pass butt-welded joint. They compared the results from the models with the experimental residual stress using hole-drilling technique and distortion measurements using three coordinate measuring technique respectively. They indicated that the model with moving heat source obtain a good prediction of welding residual stress and deformation, while the model with instantaneous heat source can provide a reasonable result for welding residual stress but poor results of distortions. However, the latter model can save a large amount of computing time. Numerical results indicate that the mesh density in the longitudinal direction has a limited influence on the results of residual stress and distortion if the instantaneous heat source model has been used. It was concluded that for industrial applications, the model with instantaneous heat source model and coarser mesh density can predict welding residual stress distribution in thick-plate joint with a large number of weld passes using a shorter computing time and a relative high accuracy.

In another study, Ding et al. [22, 23] followed this steady-state transformation approach when simulating the wire and arc additive layer manufacturing process. They demonstrated an efficient engineering FE thermo-mechanical computational procedure for simulating the production of a multi-layer wall structure. They employed a steady-state thermal model by attaching an Eulerian reference frame at the heat source in addition to thermo-elastic-plastic transient model. The modeling approach based on the steady-state thermal model showed a significant advantage of around 80–90% on the computational time compared to the conventional transient thermo-mechanical approach. According to these researchers, additional time can be saved, as using an Eulerian frame does not require as dense mesh such as the typical transient approach does. This new model produced nearly identical distortion and residual stress predictions to the transient model and experimental measurements. It was found that the peak temperatures experienced during the thermal cycles defining the effective plastic, zone determine the residual stress of that point. The stress across the deposited wall was found uniform with a small influence of the preceding layers on the following layers. The stress redistributed after unclamping with a lower value at the top of the wall than at the interface due to the bending distortion of the sample.

Although many research studies have been conducted using various FEA approaches for a variety of materials, a systems level analysis on the effect of deposition strategies on a cladded surface's functional characteristics has not been explored. In this research, an investigation is carried out on the influence of bead deposition patterns, time gap between bead depositions, and the substrate dimensions and aspect ratio on the mechanical and physical properties of the coating layer. The long-term goal of this research is to develop AM process planning tools to allow designers to explore various tool path solutions and their effect on the final part geometry and properties. The objective of this study is to investigate the effectiveness and reliability of the introduced modeling approaches to optimize the bead deposition strategies with high and uniform strength in the cladding layer with minimal physical defects. Specimens with dimensions of 75 mm × 35 mm, 75 mm × 50 mm, 100 mm × 50 mm, and 150 mm × 35 mm are investigated. Selected physical experiments were conducted, and the simulation results compared to the experimental data to determine the effectiveness of the modeling approaches.

A complementary research goal targets exploring computationally less expensive modeling techniques, the Imposed Thermal Cycle (ITC) technique and Distortion Engineering Analysis (DEA), and comparing these solutions to a traditional thermo-metallurgical-mechanical modeling technique using a moving heat source (Fig. 1) and experimental data. The deposition patterns for these rectangular specimens include cladding in the longitudinal and transverse directions, as well as spiral or fill-inward and spiral or fill-outward patterns. To explore the influence of time delays between deposition of beads, an analysis was conducted on the deposition of two beads on specimens with 100 mm and 500 mm length with time gaps of 0.5 s and 30 s. Moreover, surface cladding of a gasket with two different bead deposition patterns were studied as an example of a practical industrial application of the simulation methodologies. For the mentioned specimens, the residual stress, distortion, and hardness results were compared.

2 Establishment of the FE model

In this work, the laser cladding simulation is performed by a coupled thermal-metallurgical-mechanical analysis with the finite element software, SYSWELD. The thermal and mechanical material properties are implemented in the analysis. The resulted temperature distribution from the thermal analysis was used as an input to the mechanical analysis and metallurgical analysis. The nodal temperatures and phase transformations are calculated in a coupled manner. The thermo-physical properties depend on the temperature and the metallurgical proportions of each phase. When the internal heat source and boundary conditions applied to the heat equation, the finite element method solves a system of differential equations.

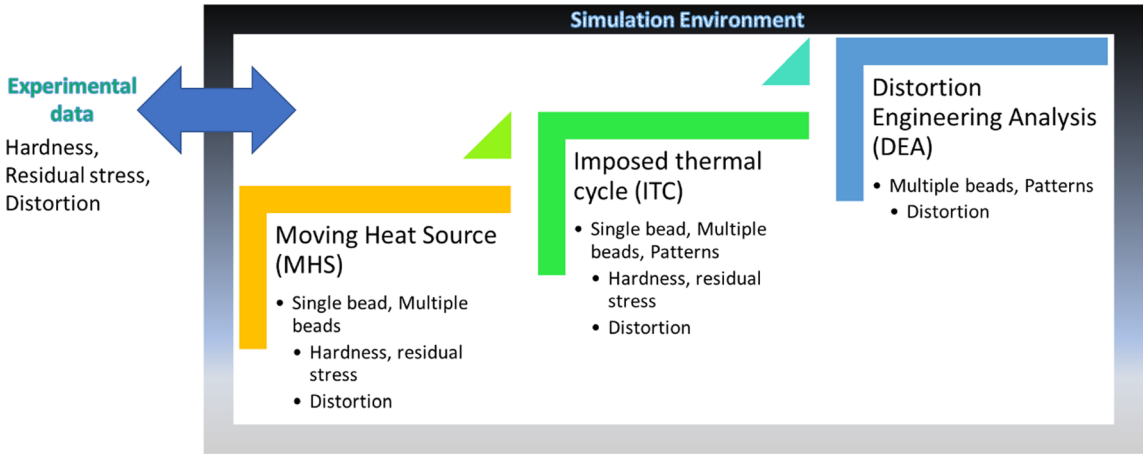

Fig. 1 Comparison of three implemented simulation approaches and their applications

2.1 Heat transfer analysis

In the thermal analysis, a transient nonlinear heat transfer analysis was performed by using an appropriate heat source model. The thermal cycle and temperature distribution during laser cladding at each node were obtained by the following equation:

$$\partial\frac{(\rho C_p T)}{\partial t} = \frac{\partial}{\partial x}\left(K\frac{\partial T}{\partial x}\right) + \frac{\partial}{\partial y}\left(K\frac{\partial T}{\partial y}\right) + \frac{\partial}{\partial z}\left(K\frac{\partial T}{\partial z}\right) + Q(x,y,z,t) \quad (1)$$

where ρ is the density of the materials (kg/m^3), C_p is the specific heat capacity (J/kg K), T is the current temperature (K), K is the temperature-dependent thermal conductivity (J/m K), Q is the internal heat generation rate (W/m^2), x, y, and z are the coordinates in the reference system (mm), and t is the time.

2.2 Thermal boundary conditions

The heat loss due to convection, q_{conv}, is described by Newton's law of cooling and Stephan-Boltzmann's law describes losses due to thermal radiation, q_{rad}, as:

$$q_{conv} + q_{rad} = -h_C(T_s - T_0) - \varepsilon\sigma\left(T_s^4 - T_0^4\right) \quad (2)$$

where h is the heat convection coefficient (W/m2 k), T_s is the surface temperature of the workpiece, T_0 is the ambient temperature (20 °C), is the surface emissivity, and σ is the Stefan-Boltzmann constant (5.67 × 10^{-8} W/m^2 k^4). In this study, the heat convection coefficient from the workpiece to the surrounding environment was 25 W/mm^2 K and the emissivity was set to a value of 0.8. The temperature in the workpiece before starting the cladding is assumed to be the ambient temperature and following the cladding process, the structure cools to room temperature.

2.3 Heat source model and metallurgical phase transformation

Three methodologies for applying the heat input were employed in the present research. In the first approach, the heat was applied using a Moving Heat Source (MHS). In the second methodology, an imposed thermal cycle (ITC) strategy is employed. The average thermal cycle of the nodes on the molten zone is calculated and the thermal computation is carried out with the resulted

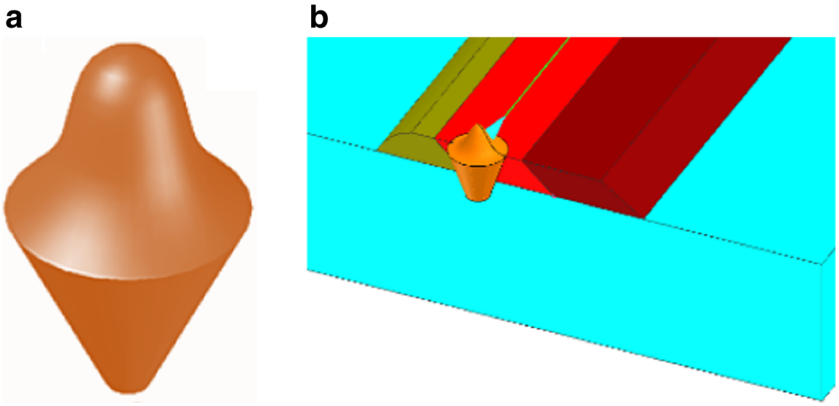

Fig. 2 **a** 3D conical Gaussian moving heat source model. **b** Heat source placed on the cladding path [13]

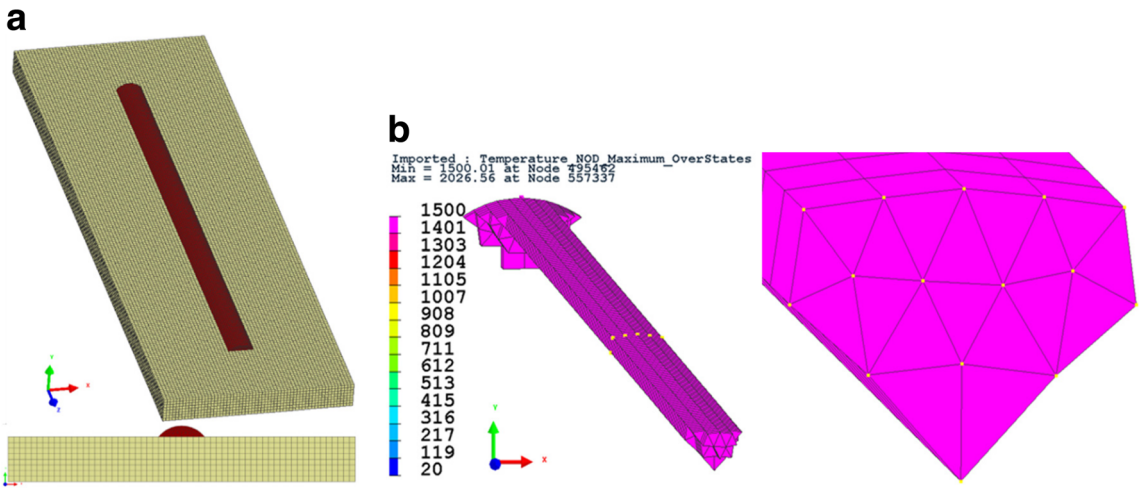

Fig. 3 **a** Geometry of a single bead specimen. **b** Melt pool region simulated by MHS technique and the nodes on the section which were used for temperature profiles to be used in ITC technique [16]

temperature profile. The third technique (DEA) is a simplified approach employed for distortion analysis.

In the first methodology, the 3D conical Gaussian moving heat source model was adopted which represents the actual laser cladding condition and can model the energy with transient thermal solution [7, 10, 13–15, 25–28]. Figure 2 depicts the view of the Gaussian moving heat source model and the way that the heat source is placed on the cladding path. The equations and needed parameters to define this heat source have been discussed in detail by the authors in Nazemi et al. [7, 13–15].

The second technique, ITC, results in much less computation time. An example of a single-track bead specimen is shown in Fig. 3a with the geometric data and process parameters presented in Table 1. The melt pool provided by the MHS technique is depicted in Fig. 3b which is used to acquire temperature profiles for the ITC technique. The temperature profiles and their average were drawn from the nodes on the cross-section of the melt pool (Fig. 4). In Fig. 5, the resulted temperature distribution in a single-track bead specimen from ITC and MHS techniques are compared while the clad bead is heating up showing the difference between their heat distribu-

Table 1 Compositions of the actual and simulations materials (wt.%)

Element	C	P	S	Si	Cr
AISI 1018	0.15–0.2	0.04	0.05	–	–
S355J2G3	(0.18)	0.035	0.035≤	≤1.0	0
P420	0.23	0.04	0.03	0.5	12.6
X20Cr13	0.16≤C≤0.25	≤0.04	≤0.03	≤1.0	12.0≤Cr≤14.0

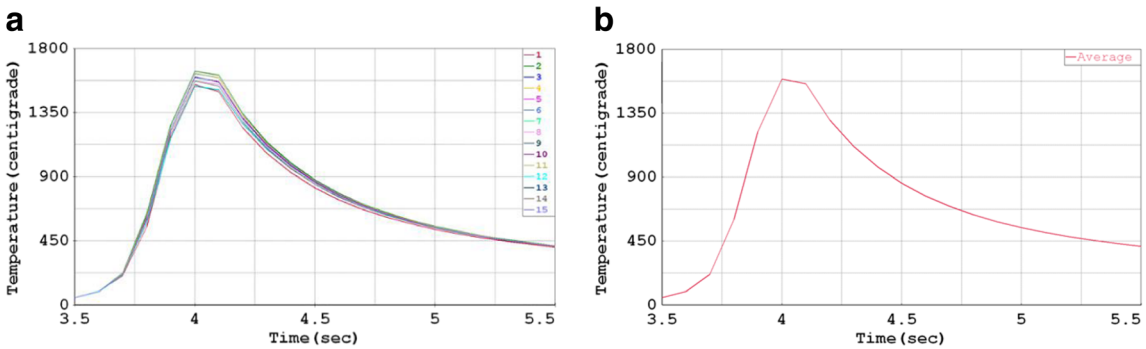

Fig. 4 Temperature profiles in the single-track specimen (**a**) on the nodes in cross-section of the melt pool (**b**) average of the profiles in the melt pool

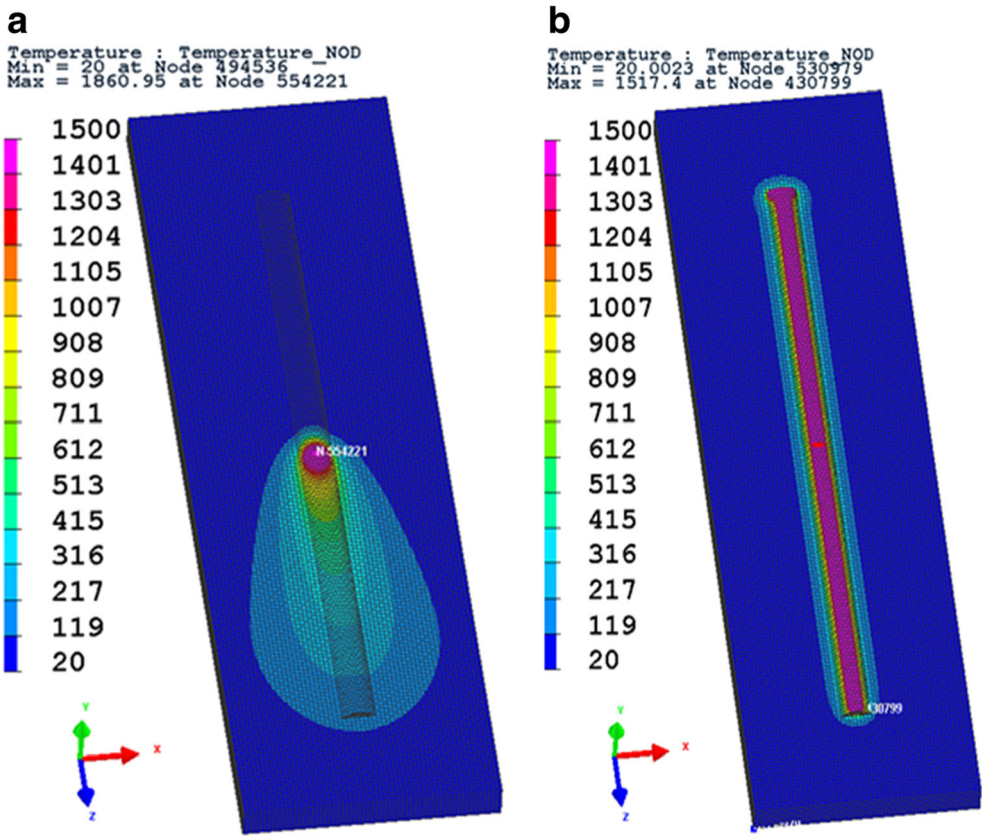

Fig. 5 Temperature contours in a single-track specimen. **a** MHS. **b** ITC

tion strategies. It shows that in the MHS, the heat source is initiated from the beginning of the bead and moves toward the end of the bead while in the ITC all the nodes in the melt pool (corresponding to the melt pool from the model with MHS) are heated up simultaneously based the temperature profile from the model with the MHS.

In the previous study carried out by the authors [16], it was shown that in the virtual simulation by using the ITC method instead of transient thermal analysis using moving heat source, the processing time for a single- and multi-track cladded specimens (three beads with 40%, 50%, and 60% overlap) with a constant heat input were reduced from 5 and 18 h to 30 min and 3 h, and from 18 h to 6 h for a multi-track cladded specimen with the transient heat input. In that study, experimental hardness and residual stress measurements were compared with the simulation results from both techniques of the MHS and ITC to assess the accuracy of the simulation solutions. Figs. 6, 7 and 8 depict a comparison between resulted hardness and residual stress results from experimental measurements and two simulation techniques for a single bead specimen and a multi-track cladded specimen with three deposited beads with 50% overlap.

In the third methodology, DEA, the basic hypothesis in this technique is that the dominant phenomenon causing cladding induced distortions is thermal shrinkage of the cladded material. The principle of software implementation is that to prescribe a fixed thermal deformation to all nodes in the cladded part. This provokes plastic deformations in the cladded area and overall distortion of the structure. The thermal shrinkage is calculated based on the following formula:

$$\textit{Thermal shrinkage} = \textit{thermal expansion coeeficient} \times \textit{temperature change} \quad (3)$$

The phase transformation during the laser cladding process was considered by the Leblond model [29] who developed an equation to replicate the CCT diagram and by using the Koïstinen-Marbürger model [30] to reproduce the cooling curve. The equations and their definitions for the phase

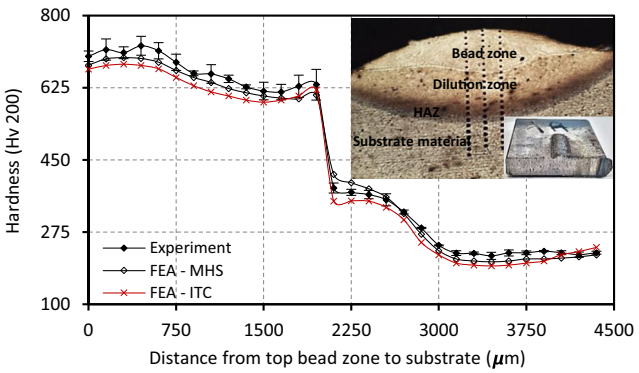

Fig. 6 A comparison of the experimental data and the two FEA solutions

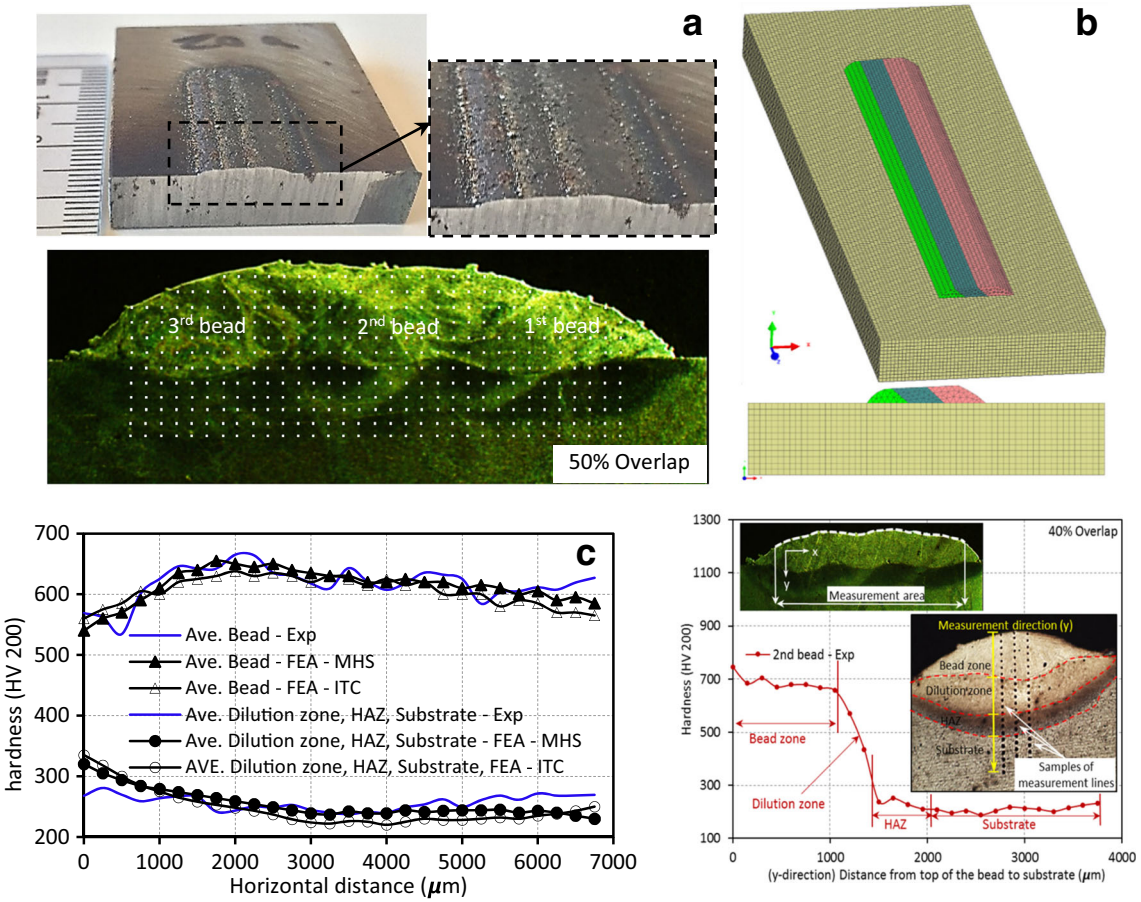

Fig. 7 **a** 3D geometry and cross-section of the specimen with three overlapped beads. **b** Average hardness values in the bead and substrate for specimens with a 50% overlap

transformation have been explained by the authors in previous research works (Nazemi et al. [7, 13–15]).

2.4 Material properties

The temperature-dependent thermo-physical and thermo-mechanical data of the clad and substrate materials in the range of ambient to the melting temperature are assigned as an input data for the analysis. The Johnson-Cook model was used for the plastic model and for temperature-dependent yield strength. Thermal properties such as the thermal conductivity and specific heat, as well as mechanical properties such as Young's modulus, yield strength, and strain-hardening curves were discussed by the authors in previous research studies in [7, 14, 15]. The material properties used in the model for the clad and substrate were those provided in the software database for the materials X20Cr13 and S355J2G3 [7, 14, 15] with chemical

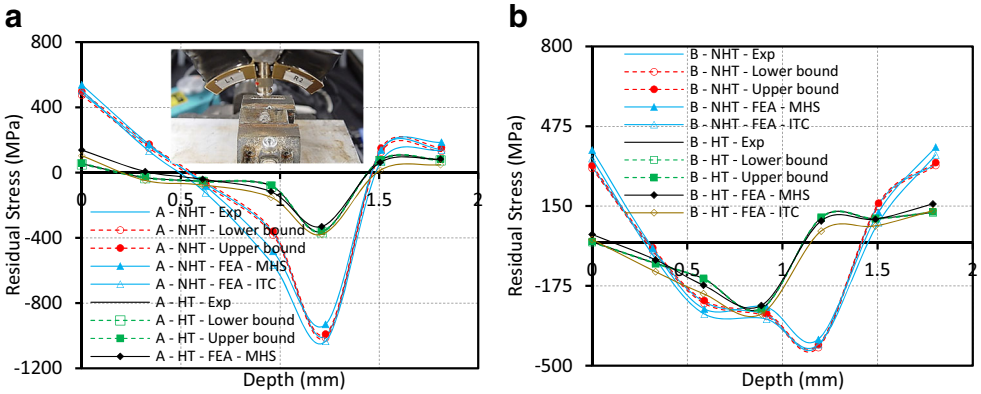

Fig. 8 Transverse residual stresses from experiment and both techniques of simulation (MHS and ITC) through the depth for non-heat-treated and heat-treated specimens. **a** Specimen A. **b** Specimen B (experimental data for **a**, **b** adapted from [13])

Table 2 Cladding process parameters

Specimen	Single bead	Three overlapped beads	Surface cladding
Powder feed rate (gr/min)	30	20	20
Laser power (kW)	2.5	2.5	2.5
Focal length of lens (mm)	400	400	400
Laser speed (mm/s)	10	10	10
Contact tip to work-piece distance (mm)	23	23	23

Table 3 Average shape parameters of specimens (mm)

50% overlap	Width	Height	Penetration
Average	8.43	1.36	0.33
STD	0.45	0.47	0.25

compositions almost identical to the chemical compositions of SS P420 and AISI 1018 (Table 1).

2.5 Meshing and constraints

The geometrical dimensions of specimens were obtained from experimental cross-section macrograph of the clad specimens at the mid-length section [13]. The cladded component geometry was modeled using three types of elements including 3D 8-noded hexahedrons solid elements for the substrate and 6 nodded tetrahedrons solid elements for the clad, 2D 4-noded elements for the surfaces for the heat dissipation through convection and radiation, and 1D 2-noded elements for the clad paths. Considering the computing accuracy and time efficiency, a denser mesh was used for the cladding, while a coarse mesh was adopted for the substrate.

3 Experimental setup

The substrate and clad powder materials were chosen as AISI 1018 cold rolled structural steel and P420 stainless steel to be consistent with previous studies by the authors [2, 7]. Experimental studies were carried out on specimens with a single bead, three beads, and multiple deposited beads. The chemical composition of the clad bead and substrate materials are depicted in Table 1. Average shape parameters of the clad beads and cladding process parameters values for specimens including laser power, the focal length of the lens, and contact tip to workpiece distance parameters are depicted in Tables 2 and 3. The cladding equipment used was a Ytterbium laser system containing a robotic arm equipped with a nozzle assembly which provides the laser spot size of 4.3 mm using a 4 kW fiber optic laser. The powders were delivered by an Argon carrier gas as a conveying media and to protect the molten pool from oxidization. The clad powder is heated when it is injected into the laser beam, which is discharged onto the substrate. Meanwhile, the laser beam locally heats the substrate to develop a molten pool. Thereafter, the surface tension gradient drives the fluid flow within the molten pool so that the deposited powder particles are mixed rapidly.

3.1 Hardness measurement

Mechanical properties in the laser cladded area were investigated using microhardness measurements. Microhardness measurements were conducted by a Buehler Vickers microhardness tester using a load of 200 m and a loading time of 12 s.

For the single bead specimen, the loads were applied vertically in the center of the bead keeping 150 μm distance from each other through the top to bottom of the bead, full dilution and HAZ, and part of the substrate materials. Two other vertical lines of loads were applied at 250 μm distance from both sides of the first loading line (Fig. 6). The values of the microhardness were averaged by 3 points of measurements taken from the previously mentioned three vertical measurement lines for single- and multi-track cladded specimens. For the multi-track specimen, an additional horizontal measurement was conducted close to the top of beads, in the middle, and on the substrate level.

Measurements on specimen with three beads with 50% overlapping were carried out at the mid-length section of the samples. Measurement locations are shown with white dots on macro-etched pictures of specimens in Fig. 7a. In the horizontal direction, the starting point for measurements was from the point that the dilution between the first clad bead and substrate begins (bonding region) to the end of the bonding region of the third bead. In the vertical direction, measurements were conducted from top of the beads to the HAZ below the substrate/bead

Table 4 Operating parameters for the X-ray diffraction measurements

X-ray elastic constant	Crystallographic plane	Brag angle	Gain material	Aperture	Oscillation(s)	Collection time
25,578.95 ksi	{211}	155.1°	Titanium-Beta	1.0 mm-round	Beta 4.0 °	4 min

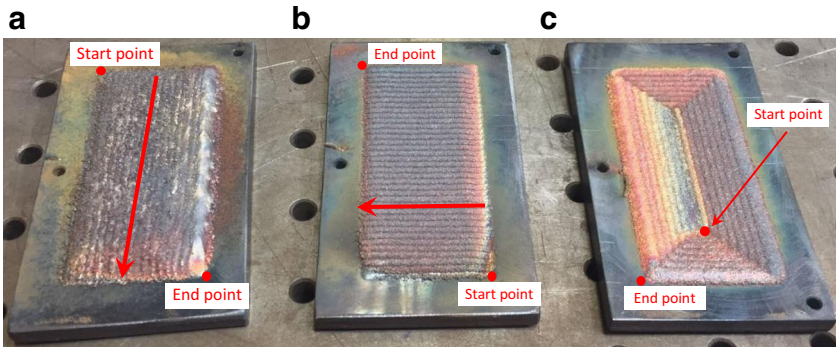

Fig. 9 Experimental laser cladded specimens with various deposition patterns. **a** Longitudinal pattern. **b** Transverse pattern. **c** Spiral pattern

interface. Measurements were recorded at each 250 μm horizontal distances and 150 μm vertical distances. Number of measurement points in horizontal direction was 28 measurements.

The hardness and residual stress profiles for the single-track cladded specimen and a specimen with three overlapped beads from the top of the bead through the dilution zone, HAZ, and substrate materials are depicted in Figs. 6, 7. In these figures, the experimental results were compared with the simulation results of the MHS and ITC techniques which show a good correlation.

3.2 Residual stress measurement

The residual stress profiles were measured using the X-ray diffraction technique. X-ray diffraction technique allows for rapid measurements of strains inside components and uses the changes in the spacing of the internal crystal lattice planes as an atomic strain gauge. In the current study, the residual stress measurement was conducted using the Proto X-ray diffraction system (Lab 002/LXRD 06024) and the operating parameters for the X-ray diffraction measurements are presented in Table 4. The measurements were done at the center of the bead

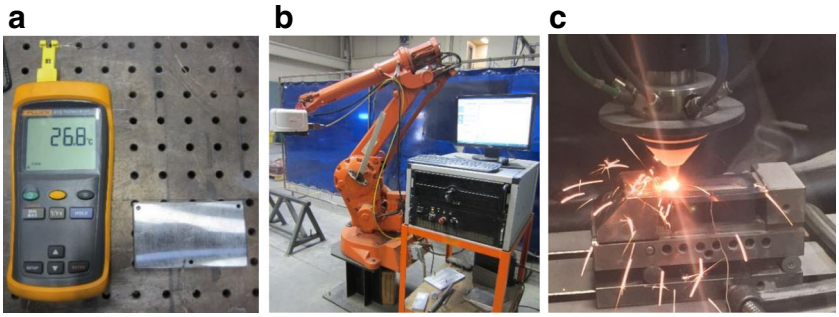

Fig. 10 **a** Thermocouple wire tack welded to the specimen. **b** Laser cladding torch and a specimen with spiral deposition pattern during laser cladding. **c** Robotic fiber optic laser marking machine used for engraving the mapping on back of specimens

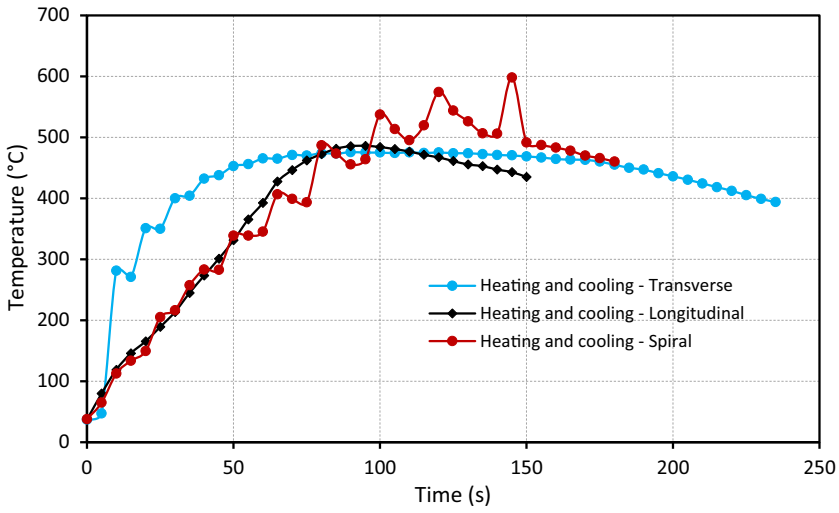

Fig. 11 Temperature measurements using thermocouple during laser cladding of specimens with deposition patterns of transverse, longitudinal, and spiral

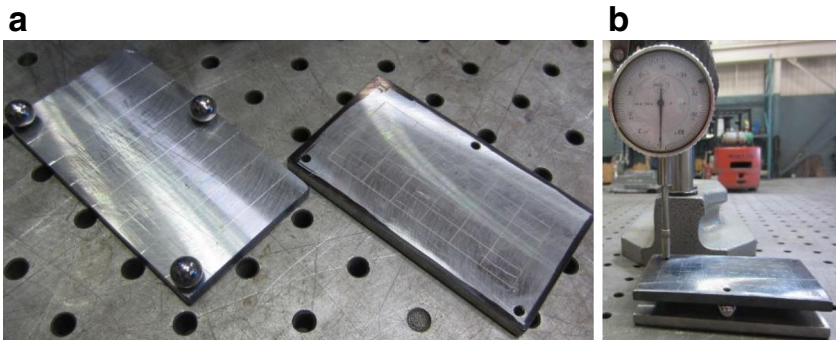

Fig. 12 **a** Mapping on the back of a specimen used for distortion measurements ball bearing, and specimen (**b**) probe height gage used for distortion measurements

and perpendicular to the bead line at the surface and six subsurface points with varying depth. Figure 8a shows the single-track cladded specimen under X-ray measurement. The residual stress profiles for the single-track cladded specimen from the top of the bead through the dilution zone, HAZ, and substrate materials are depicted in Fig. 8. In this figure, the

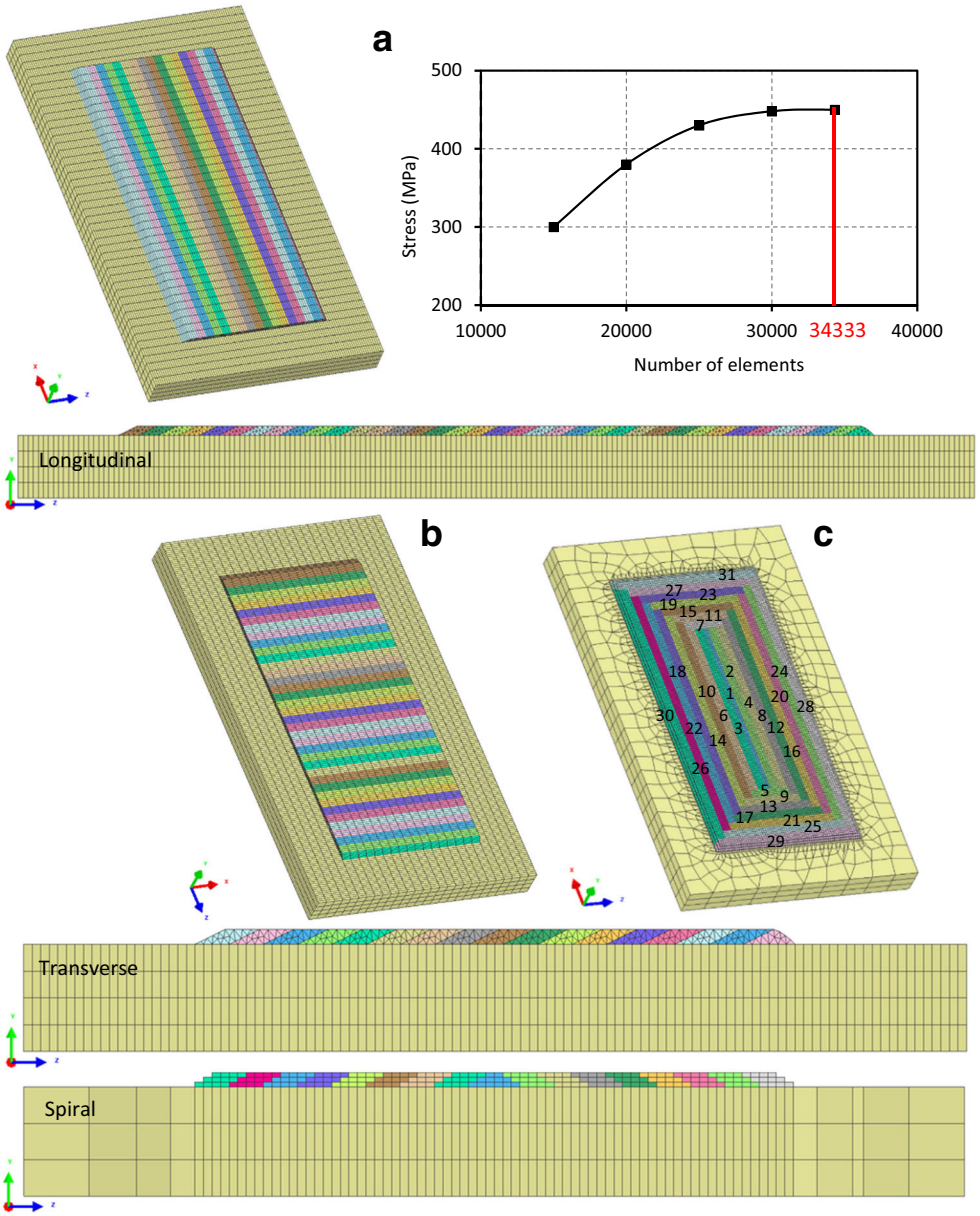

Fig. 13 3D geometry and cross-section of the **a** specimen with longitudinal bead deposition and convergence study on number of elements, **b** specimen with transverse bead deposition, and **c** specimen with spiral bead deposition

experimental results were compared with the simulation results of the MHS and ITC techniques which show a good correlation.

3.3 Distortion measurement

Experimental specimens were used to compare the effect of different patterns of bead deposition on the distortion distribution. The experimentally measured distortion results were further used to validate the simulation model. Once the confidence was gained with respect to the accuracy of the simulation techniques, the models were further used to extend the study for a wide variety of bead deposition patterns and different cladded parts.

Based on a preliminary simulation to find the most applicable and distinct deposition outlines, three specimens with various patterns of cladding were chosen and prepared. The selected patterns included transverse, longitudinal, and spiral bead depositions as shown in Fig. 9. The cladded surface dimensions for the specimens were 35 mm × 75 mm with a 10 mm margin on each side (55 mm × 95 mm). A thermocouple device was used to measure the temperature data during the cladding and cooling. The thermocouple wires were attached to the specimens, close to the left holes in Fig. 10a, by a tack weld in the outer margin of the cladding surface in order to prevent interference with the cladding process. Distortion measurement locations on the specimens were mapped by a robotic fiber optic laser marking machine (Fig. 10b). Figure 10c depicts the laser cladding of the specimen with spiral bead

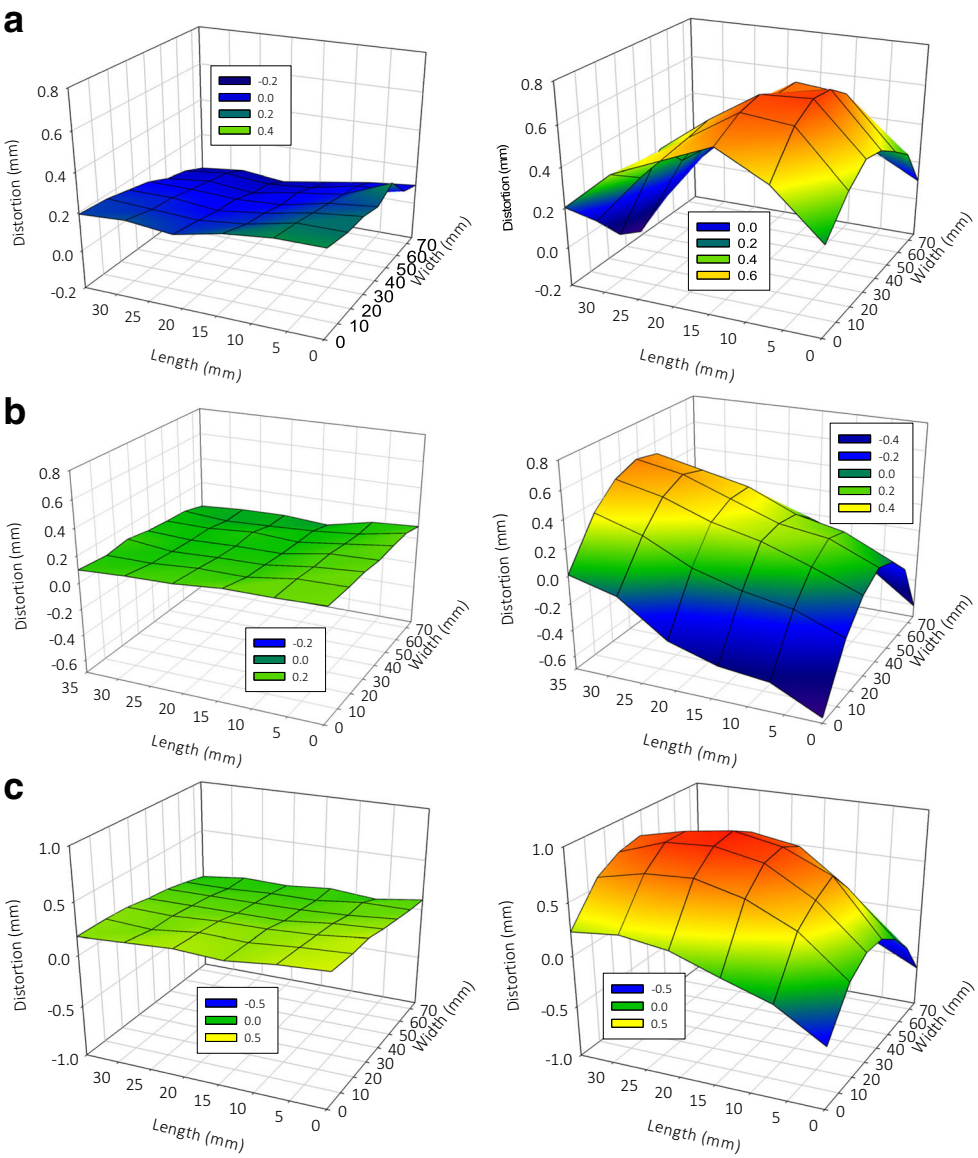

Fig. 14 Experimentally measured distortions before cladding (in the left) and after cladding (in the right) on specimens with various patterns of cladding. **a** Longitudinal. **b** Transverse. **c** Spiral

Table 5 Experimentally and numerically measured maximum values of distortions in the specimens similar to the experimented specimens

Deposition pattern	Flatness (mm)				
	Experiment	Simulation (DEA)	Error	Simulation (ITC)	Error
Transverse	0.475 [− 0.706]: 1.181	0 [− 1.181]: 1.237	4.7%	0.028 [− 0.790]: 0.820	31%
Longitudinal	0.554 [− 0.305]: 0.859	0 [− 1.115]: 1.115	30%	0.175 [− 1.308]: 1.483	73%
Spiral	0.800 [− 0.711]: 1.816	0 [− 2.090]: 2.090	15%	0.018 [− 1.598]: 1.616	11%

deposition pattern. Temperature profiles are shown in Fig. 11 which indicates that in the recorded location, temperature fluctuations are observed in the transverse and spiral patterns but not in the longitudinal pattern.

3.4 Distortion measurement technique

Distortion measurements were conducted at 42 locations on the face of the specimens which were not cladded (Fig. 12a). In order to have the same reference level for distortion measurements, the basic 3-2-1 fixturing principle was used. Three 3 mm holes drilled through the plate were created at the same three locations on each specimen (Fig. 12a). Ball bearings with a diameter of 9 mm were placed underneath the holes on the surface plate (Fig. 12b). This established a planar surface for reference and a stable, static method for locating all samples. Distortion measurements were carried out on specimens before and after the cladding using a probe indicator as shown in Fig. 12b. The 3D geometry and the mid-length cross-section of the simulated specimens are shown in Fig. 13. The investigated specimens have the same geometric specifications as the experimental samples (Fig. 9).

The convergence study on the mesh size for a suitable agreement between the accuracy and computational running time was conducted by evaluating the variation of the achieved maximum residual stress versus the number of elements. The residual stress was chosen as the criteria as this is an analysis response after the thermal-metallurgical-mechanical interactions

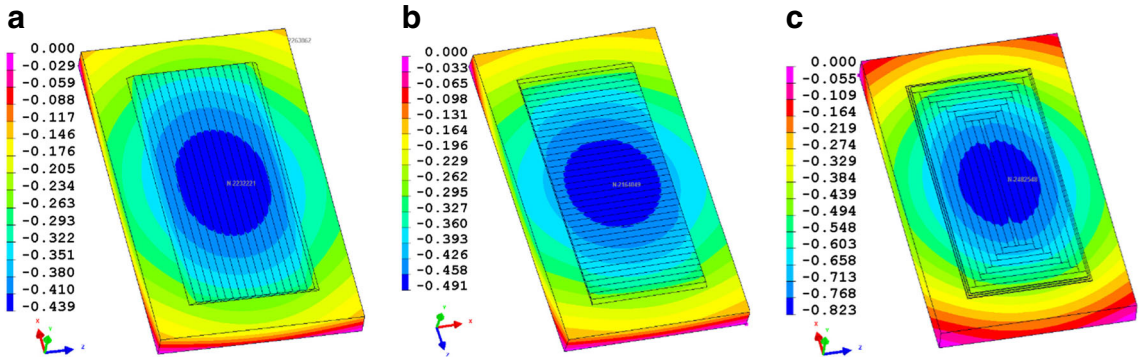

Fig. 15 Simulated distortion results (in inches) using DEA on specimens with various patterns of cladding. **a** Longitudinal. **b** Transverse. **c** Spiral

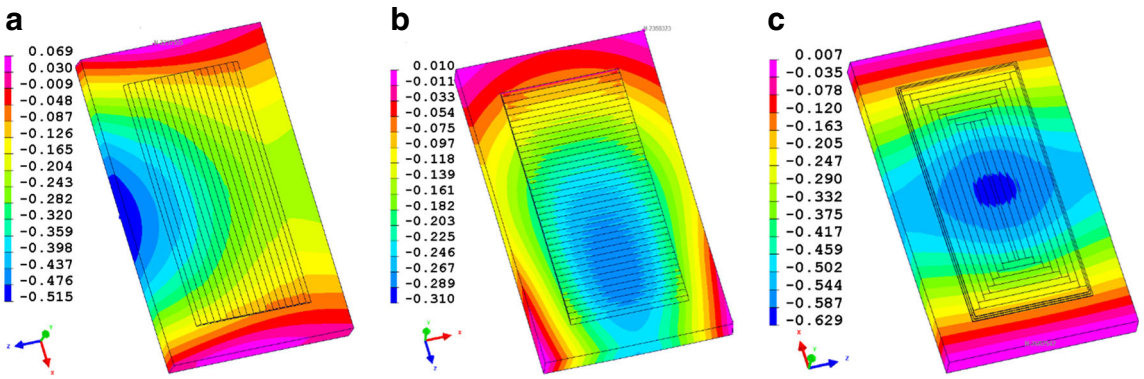

Fig. 16 Simulated distortion results using ITC on specimens with various patterns of cladding. **a** Longitudinal. **b** Transverse. **c** Spiral

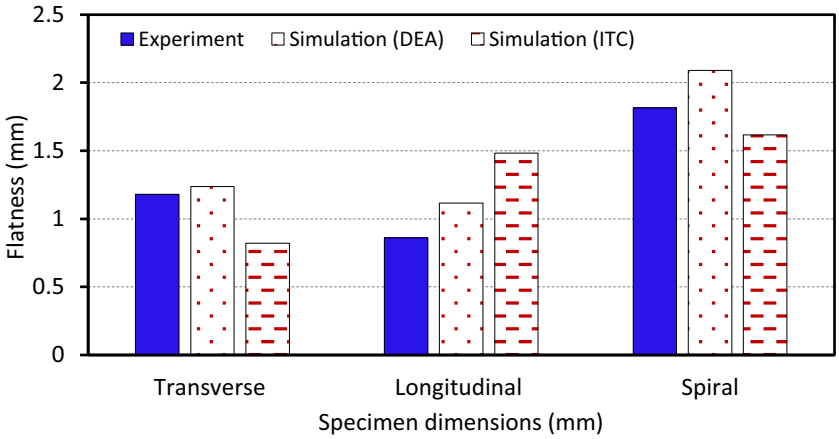

Fig. 17 Comparison of flatness values for the specimens in Fig. 1, measured experimentally, as well as DEA and ITC techniques

are completed. As an example, the result of convergence study for the surface cladded specimen with longitudinal bead deposition is depicted in Fig. 13a. This shows the variation of the maximum residual stress value becoming insignificant when increasing the number of 3D elements to more than 34,333.

Experimental distortion measurement results are shown in Fig. 14 and Table 5. The measurement results indicate that

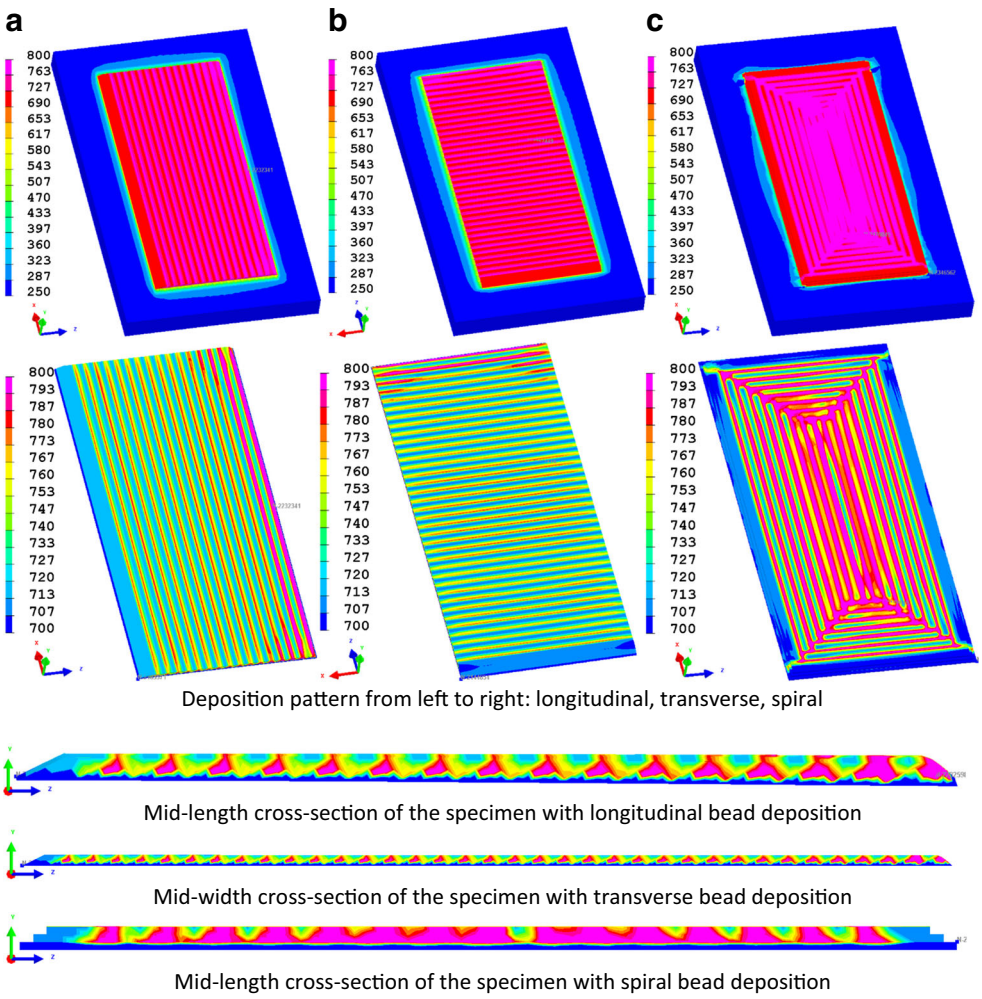

Fig. 18 Simulated hardness contour using ITC on specimens with various patterns of cladding. **a** Longitudinal. **b** Transverse. **c** Spiral

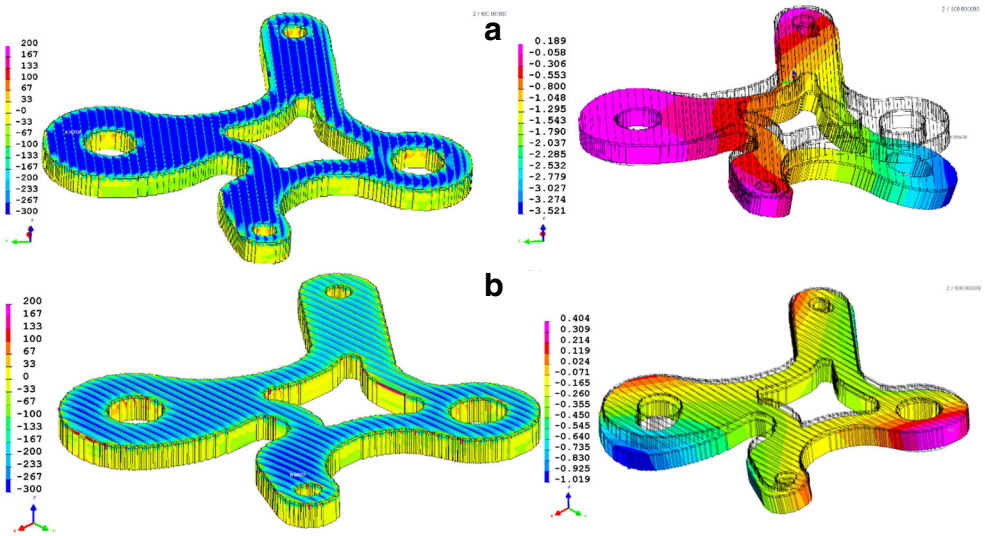

Fig. 19 Distortion results in a laser cladded gasket specimen with two different patterns of bead deposition using DEA technique (distortion values were scaled 10 times larger)

longitudinal deposition pattern and the spiral deposition patterns cause the minimum and maximum distortion in the cladded specimen respectively. The total flatness values for transverse, longitudinal, and spiral patterns of cladding are 1.181 mm, 0.859 mm, and 1.816 mm. The distortion distribution pattern also varies. The transverse and longitudinal bead pattern depositions have a concave shape in the direction of cladding and spiral bead deposition pattern has a bowl shape due to the bead deposition in both transverse and longitudinal directions. Experimental distortion measurements were compared with the numerical results from the two techniques for ITC and DEA solution methodologies in Figs. 15 and 16, as well as the Table 5. From the figures, it can be concluded that DEA technique gives reliable results regarding the values and pattern of distortion. However, the ITC gives less accurate results, but it shows relatively acceptable patterns of distortion. The error for the flatness values of transverse, longitudinal, and spiral patterns using DEA are 4.7%, 30%, and 15% comparing to 31%, 73%, and 11% error for the ITC technique. The results from experimental measurements, simulation with DEA technique, and simulation with ITC technique are compared in a graph in Fig. 17.

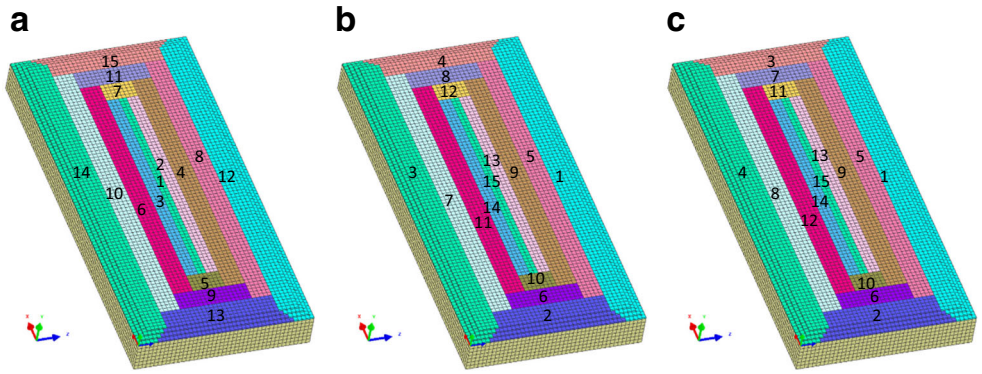

Fig. 20 Various simulated patterns of spiral disposition on specimens with dimensions of 75 mm × 35 mm which were used for comparison of residual stress results using ITC technique. **a** Filling out-ward. **b** Filling in-ward. **c** Filling diagonally

Table 6 Maximum distortions (DEA) and residual stresses (ITC) in specimens with a size of 75 mm × 35 mm and spiral beads in Fig. 19

Deposition pattern	Flatness (mm)	Max mean tensile residual stress (MPa)	Max mean compressive residual stress (MPa)
Pattern 1	0.117 [− 1.976]: 2.093	291	− 377
Pattern 2	0.015 [− 1.245]: 1.260	327	− 358
Pattern 3	0.000 [− 1.052]: 1.052	472	− 398

Pattern of filling (1) out-ward (2) in-ward (3) diagonally

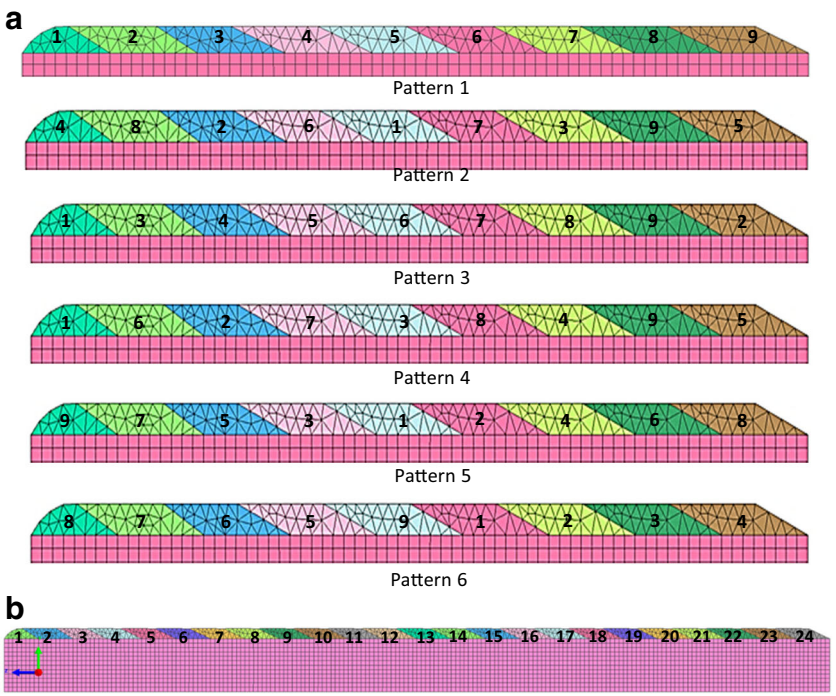

Fig. 21 Various simulated patterns of bead disposition on specimens with dimensions of 75 mm × 35 mm which were used for comparison residual stress results using ITC technique. **a** Longitudinal. **b** Transverse

Table 7 Maximum distortions (DEA) and residual stresses (ITC) in the 75 mm × 35 mm specimen with longitudinal beads in Fig. 20

	Flatness (mm)	Residual stress (MPa)					
		Transverse		Longitudinal		Mean	
Pattern		T	C	T	C	T	C
1	0.000 [− 1.361]: 1.361	375	− 535	538	− 446	275	− 327
2	0.000 [− 1.331]: 1.331	348	− 493	794	− 390	284	− 288
3	0.000 [− 1.377]: 1.377	381	− 524	819	− 429	285	− 312
4	0.000 [− 1.359]: 1.359	356	− 475	774	− 380	279	− 280
5	0.000 [− 1.138]: 1.138	630	− 518	886	− 415	397	− 306
6	0.000 [− 1.275]: 1.275	725	− 518	919	− 418	439	− 307

T: Tensile, C: Compressive

Flatness (DEA) in the specimen with transverse beads is 0.000 [− 1.732]: 1.732

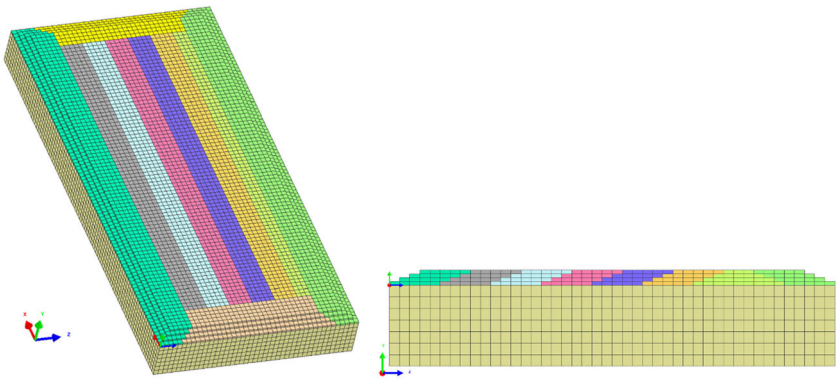

Fig. 22 Specimen with outer contour and longitudinal bead deposition filling

Table 8 Maximum distortions (DEA) and residual stresses (ITC) in specimens with the size of 75 mm × 35 mm with spiral outer contour and longitudinal filling

Pattern	Flatness (mm)	Max mean tensile residual stress (MPa)	Max mean compressive residual stress (MPa)
1	0.096 [− 1.095]: 1.092	392	− 351
2	0.096 [− 1.448]: 1.051	456	− 332

Pattern 1, outer contour first, then longitudinal deposition filling

Pattern 2, longitudinal deposition filling first, then outer contour

4 Model application

In this section, the simulation results of hardness, distortion, and residual stress are discussed and compared for specimens with the various substrate and clad sizes, as well as patterns of bead deposition.

4.1 Hardness results using ITC

It was shown in Figs. 6 and 7 that the ITC technique produces an accurate and acceptable prediction of hardness values. Therefore, this technique was adopted to calculate the hard-

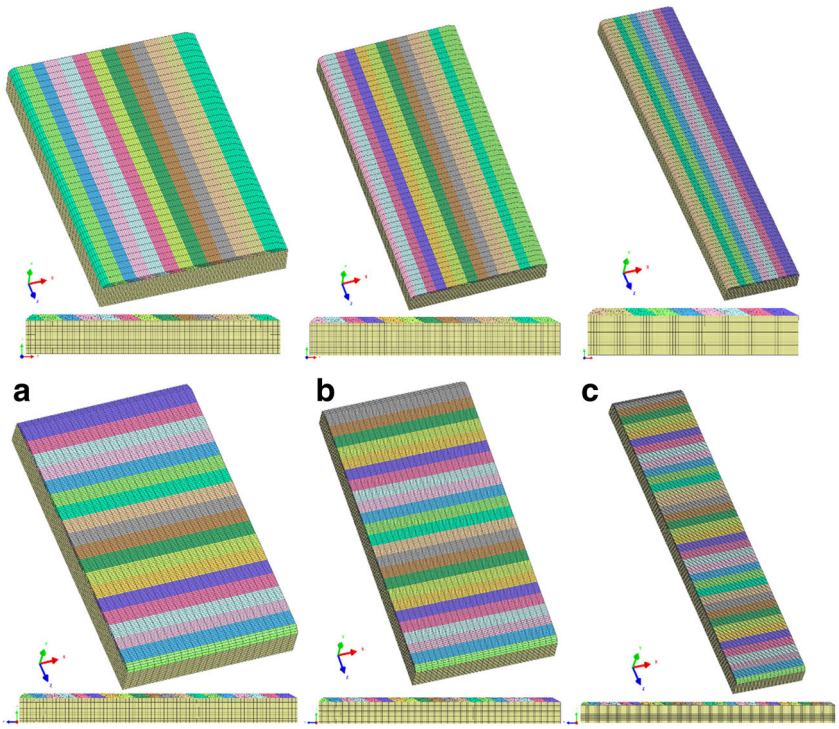

Fig. 23 Specimens with transverse and longitudinal bead deposition patterns with various sizes. **a** 75 mm × 50 mm. **b** 100 mm × 50 mm. **c** 150 mm × 35 mm

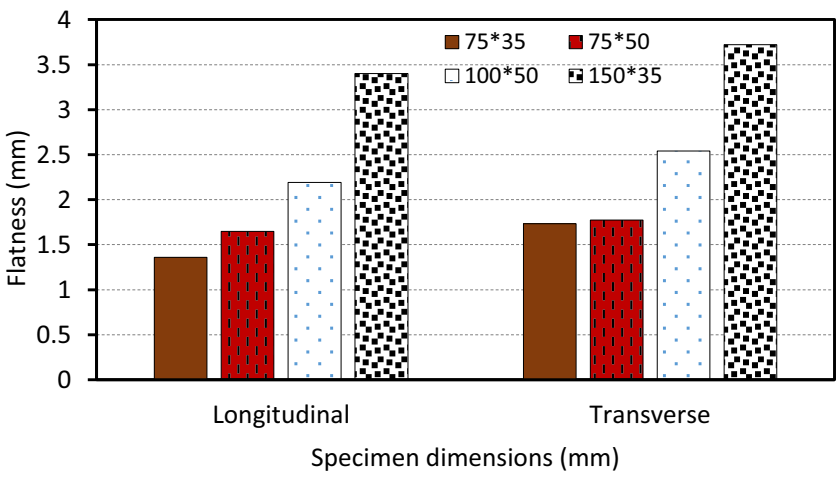

Fig. 24 Flatness values for specimens with transverse and longitudinal bead deposition patterns and for specimens with various sizes (DEA)

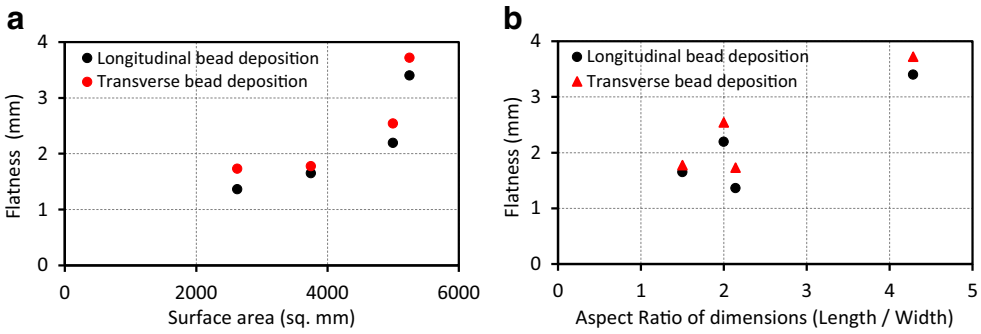

Fig. 25 **a** Flatness values for specimens with various aspect ratio of dimensions (length/width) (DEA). **b** Flatness values for specimens with various surface area (DEA)

Table 9 Maximum distortions in specimens with various sizes (DEA)

Dimension (mm)	Flatness (mm)	
	Longitudinal beads	Transverse beads
75 × 50	0.000 [− 1.648]: 1.648	0.000 [− 1.775]: 1.775
100 × 50	0.000 [− 2.192]: 2.192	0.000 [− 2.540]: 2.540
150 × 35	0.000 [− 3.401]: 3.401	0.000 [− 2.540]: 2.540

ness contour on the surface cladded specimens with various types of bead depositions and to compare the effect of cladding pattern on values and variation of hardness in the cladded area and substrate. The simulated hardness contours of the specimens with longitudinal, transverse, and spiral patterns of cladding are shown in Fig. 18 which indicates that the specimens with the spiral and transverse patterns of cladding have the highest and lowest maximum hardness values. In addition, the spiral pattern of cladding creates more uniform hardness contour in the clad area.

4.2 Distortion results using ITC and DEA

The DEA technique was further employed to study the effect of bead deposition patterns on distortion distribution and values in a gasket part shown in Fig. 19 with a large number of cladding beads which reveals the effect of bead deposition pattern on values and distribution of distortions.

Effect of bead deposition pattern was explored by comparing three different patterns including out-ward, in-ward, and diagonal filling (Fig. 20) with the bead geometry of 8 mm width, 1 mm height, and 50% overlap. The results from Table 6 indicate that the out-ward and diagonal patterns

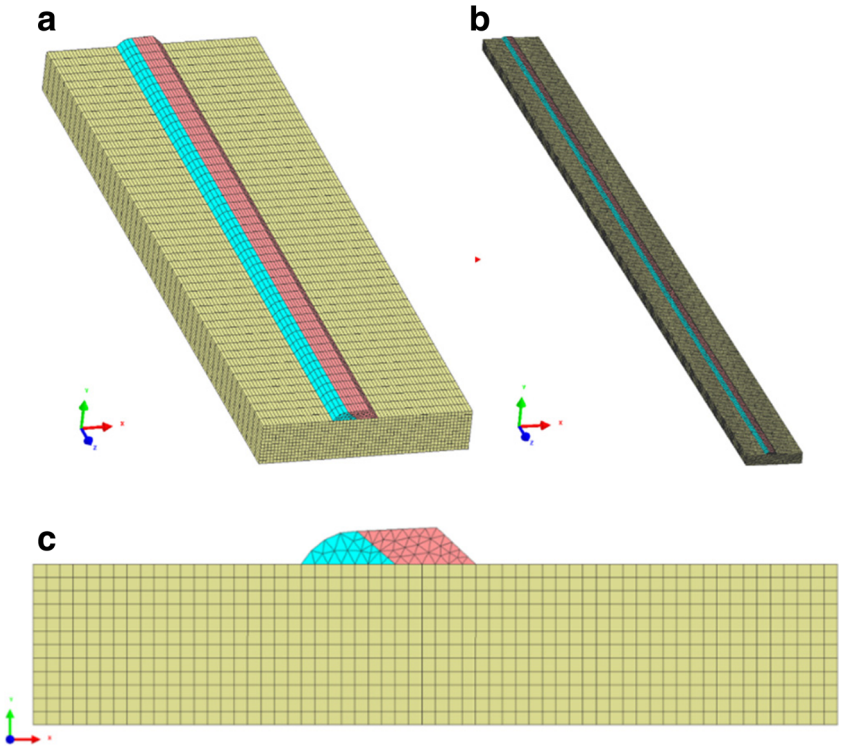

Fig. 26 Specimens with two 50% overlapped beads (**a**). 3D view of specimen with the size of 100 mm × 30 mm × 6 mm (**b**). 3D view of specimen with the size of 500 mm × 30 mm × 6 mm (**c**)

Table 10 Maximum distortions (DEA) in specimens with two 50% overlapped beads with the sizes of 100 mm × 35 mm and 500 mm × 35 with two different time gaps between two beads

Specimen length	100 mm		500 mm	
Time gap	0.5 s	30 s	0.5 s	60 s
Flatness (mm)	0.000 [− 0.627]: 0.627	0.000 [− 0.627]: 0.627	0.000 [− 3.604]: 3.604	0.000 [− 3.604]: 3.604

caused the highest (2.093 mm) and lowest (1.052 mm) values of flatness. In another study, the effect of the order of longitudinal bead depositions on maximum distortion values in specimens with dimensions of 75 mm × 35 mm and similar bead geometry and overlap to the previous case were investigated by the DEA technique (Fig. 21). From the results in Table 7, it can be concluded that the patterns 5 and 3 caused the lowest and highest flatness values. Another pattern of bead deposition that was considered was the pattern with outer contour and longitudinal filling for the specimen with the size of 75 mm × 35 mm (Fig. 22) and similar bead geometry and overlap as the previous case. Two patterns were studied with outer contour first and longitudinal filling first. The distortion result in Table 8 reveals that starting with the outer contour caused a higher value of flatness than starting with the longitudinal filling.

The influence of substrate dimensions and aspect ratio on the mechanical and physical properties of the coating layer was studied. The study was conducted on specimens with dimensions of 75 mm × 35 mm, 75 mm × 50 mm, 100 mm × 50 mm, and 150 mm × 35 mm (Fig. 23) with the bead geometry of 8 mm width, 1 mm height, and 50% bead overlap. The resulted flatness in these specimens and the specimen with 75 mm × 35 mm (Pattern 1 in Fig. 21a, b) are shown in Figs. 24 and 25 and Table 9. It is concluded that with larger sizes and cladded area, distortion values increase. Moreover, the effect of the time gap between bead deposition was investigated by comparing the flatness in a specimen with 100 mm and time gaps of 0.5 s and 30 s, as well as a specimen with 500 mm length and time gaps of 0.5 s and 60 s. The geometry of specimens are shown in Fig. 26. The results in Table 10 reveal that the time gap does not have a significant effect on the developed distortions.

Table 11 Maximum mean residual stresses (MPa) in the specimens in Fig. 1 using ITC technique

Deposition pattern	Tensile	Compressive
Transverse	355	− 425
Longitudinal	362	− 457
Spiral	572	− 1718

4.3 Residual stress results using ITC technique

It was shown previously that the ITC technique gives an acceptable result for prediction of residual stress. This technique was further used to determine the residual stresses in the surface cladded specimens. In Table 6, mean residual stress results for three different spiral bead deposition patterns were compared (Fig. 20). This residual stress results in this table reveal that the diagonal filling pattern induced the highest values of mean compressive and tensile residual stresses. The out-ward filling and in-ward bead deposition patterns induced the lowest values of mean tensile and compressive residual stress. In Table 7, maximum tensile and longitudinal residual stresses in the 75 mm × 35 mm specimen with six longitudinal patterns of bead deposition are depicted. Patterns 6 and 1 developed the highest and lowest mean tensile residual stress and patterns 1 and 4 induced the highest and lowest mean compressive residual stress.

Table 11 depicts the mean residual stress results calculated by the ITC technique in the specimens similar to the experimental ones with three patterns of bead deposition. From this table, it can be concluded that the spiral and transverse patterns of cladding caused the highest (− 1718 MPa, 572 MPa) and lowest (− 425 MPa, 355 MPa) values of mean compressive and tensile residual stresses. In addition, the transverse and longitudinal residual stresses in the mentioned specimens with transverse and longitudinal bead depositions were compared in Table 12 that reveals that transverse bead deposition developed lower values of residual stresses. The comparison of residual stresses in specimens with various sizes (Table 13) reveals that highest residual stress was observed in the specimen with the dimensional aspect ratio of 4.28 (150 mm/35 mm) and the lowest residual stress was observed in the

Table 12 Maximum residual stresses (MPa) in the specimen with the size of 75 mm × 35 mm (ITC)

Transverse bead deposition				Longitudinal bead deposition			
Transverse		Longitudinal		Transverse		Longitudinal	
T	C	T	C	T	C	T	C
402	− 688	754	− 600	461	− 668	729	− 646

T: Tensile, C: Compressive

Table 13 Maximum residual stresses (MPa) in specimens with various sizes (ITC technique)

Dimensions (mm)	Longitudinal bead deposition				Transverse bead deposition			
	Longitudinal stress		Transverse stress		Longitudinal stress		Transverse stress	
	T	C	T	C	T	C	T	C
75 × 50	546	− 434	377	− 517	553	− 446	376	− 506
100 × 50	513	− 413	373	− 494	545	− 445	378	− 496
150 × 35	546	− 478	389	− 538	495	− 449	376	− 514

T: Tensile, C: Compressive

Table 14 Maximum residual stresses (MPa) and hardness (HV 200) in specimens with two 50% overlapped beads with two different time gaps between two beads (ITC)

Specimen length	100 mm				500 mm			
Time gap	0.5 s		30 s		0.5 s		60 s	
Hardness	822		821		800		804	
Tensile/compressive residual stress	T	C	T	C	T	C	T	C
Transverse residual stress	424	− 606	426	− 577	417	− 598	416	− 544
Longitudinal residual stress	1095	− 648	1223	− 648	1107	− 628	1240	− 614
Mean residual stress	467	− 432	527	− 427	473	− 425	532	− 408

specimen with the dimensional aspect ratio of 2 (100 mm/50 mm). In Table 14, the effect of the time gap between deposition of the subsequent overlapped bead was investigated for a specimen with 100 mm and time gaps of 0.5 s and 30 s, and a specimen with 500 mm length and 0.5 s and 60 s time gaps. The results indicate that a longer time gap developed higher tensile residual stresses and lower compressive residual stresses.

It is noticed that no configuration provides an ideal solution. However, by performing simulation studies for each industrial cladding project, decisions can be made by the manufacturer to achieve the desired strength and optimized residual stress and distortion in the cladded part.

5 Summary and conclusions

When performing process planning operations for general machine tool or robotic-based systems utilized for additive manufacturing, in many environments planners will modify machining tool paths. In the present study, it is clearly shown that deposition strategy influences the final results, and that additive tool paths are not the opposite of material removal tool paths. Classic 'facing' tool paths used for machining are emulated for laser cladding. Complementary research, focusing on efficient simulation methodologies, were investigated to predict hardness, residual stress, and distortion results for large-scale parts.

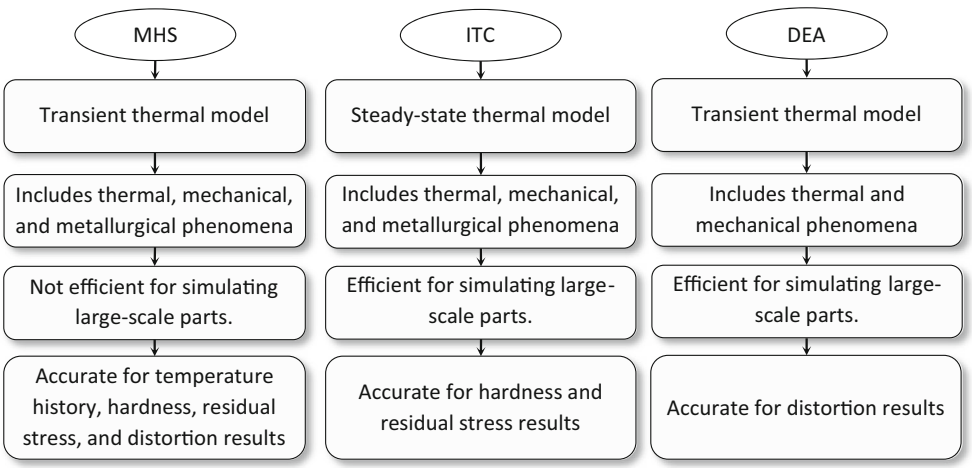

Fig. 27 Laser cladding simulation techniques in the present study and their specifications, advantages, and disadvantages

By comparing three transverse, longitudinal, and spiral bead deposition patterns, it was concluded that the spiral and longitudinal patterns of cladding bead deposition caused the highest and lowest values of distortions, as well as the highest and lowest values of mean compressive and tensile residual stresses. By investigating the effect of the time gap between subsequent overlapped beads, it was shown that the time gap does not affect the maximum distortion values in the cladded parts. However, a longer time gap increases the tensile residual stress and decreases the compressive residual stress. Therefore, rapid positioning moves can have an influence on the final results—again very different from machining.

By comparing the three spiral bead deposition patterns, it was shown that the diagonal filling pattern induced the highest values of mean compressive and tensile residual stresses. The out-ward filling and in-ward bead deposition patterns induced the lowest values of mean tensile and compressive residual stress.

The transient moving heat source model, which included all thermal, metallurgical, and mechanical interactions during heating and cooling of laser cladding process, generated the most accurate results for hardness, residual stress, and distortions. However, the computational time is long. Consequently, this approach is not practical for industrial purposes. The second technique, the imposed thermal cycle model, is carried out by steady-state thermal analysis while considering the thermal, metallurgical, and mechanical phenomena. The results are acceptable for hardness and residual stress, but the distortion results are not accurate. However, the distortion pattern correlates relatively well with experimental observations. In the third methodology, the distortion engineering analysis, phase transformations are not taken into consideration and the hypothesis is that the major phenomenon causing laser cladding induced distortions is the effect of thermal expansion coefficient. The Fig. 27 flowchart for the laser cladding simulations summarizes the advantages and disadvantages for each technique.

The future studies will target improving the ITC technique to be able to give accurate results for distortions, as well as residual stresses, and hardness, and to explore simulating large, complex case studies.

Acknowledgments This research is funded by the Ontario Center of Excellence Collaborative Research program, Natural Sciences and Engineering Research Council of Canada through the Discovery Grant, and Mitacs. The authors would like to thank the industry sponsor, Mr. Robert Hedrick of Camufacturing Solutions Inc. for the partial funding and resources he has provided for this research project.

Nomenclature 3D, 3 dimensional; CCT, continuous cooling transformation; C_p, specific heat capacity (J/kg.K); h, heat convection coefficient (w/m^{2}K); k, thermal conductivity of the material (W/mm.K); Q, volumetric heat flux rate from heat source (W/m^3); q, heat flux vector (W/mm^2); q_0, heat flow density (W/m^3).; r_0, r_e, determinate 3D Gaussian radiuses (m); T, temperature (°K); z_i, z_e, determinate length of 3D Gaussian (m); x, y, z, Cartesian coordinate (mm); ρ, density of the material (kg/mm^3); ∇, spatial gradient operator; ε , emissivity; σ, Stefan-Boltzman constant (W/m^{2}k^4)

References

1. Cao S, Gu D, Shi Q (2017) Relation of microstructure, microhardness and underlying thermodynamics in molten pools of laser melting deposition processed TiC/Inconel 625 composites. J Alloys Compd 692:758–769
2. Nazemi N, Urbanic RJ, (2017) A numerical analysis approach to evaluate hardness and distortion for selected multi-track laser cladding configurations: P420 steel beed deposition on mild steel. ASME International Mechanical Engineering Congress and Exposition, November 3–9, Tampa, FL, USA
3. Weman K (2011) Welding processes handbook. Elsevier, Amsterdam, pp 188–190
4. Salonitis K, D'Alvise L, Schoinochoritis B, Chantzis D (2016) Additive manufacturing and post-processing simulation: laser cladding followed by high speed machining. Int J Adv Manuf Technol 85:2401–2411
5. Fallah V, Alimardani M, Corbin SF, Khajepour A (2011) Temporal development of melt-pool morphology and clad geometry in laser powder deposition. Comput Mater Sci 50:2124–2134
6. Hofman JT, Lange DF, Pathiraj B, Meijer J (2011) FEM modeling and experimental verification for dilution control in laser cladding. J Mater Process Technol 211(2):187–196
7. Nazemi N, Urbanic J (2016) A finite element analysis for thermal analysis of laser cladding of mild steel with P420 steel powder. ASME International Mechanical Engineering Congress and Exposition, November 11–17, Phoenix, AZ
8. Santhanakrishnan S, Kong F, Kovacevic R (2011) An experimentally based thermo-kinetic hardening model for high power direct diode laser cladding. J Mater Process Technol 211(7):1247–1259
9. Zhang Z, Farahmand P, Kovacevic R (2016) Laser cladding of 420 stainless steel with molybdenum on mild steel A36 by a high power direct diode laser. Mater Des 109:686–699
10. Chew Y, Pang JHL, Bi G, Song B (2015) Thermo-mechanical model for simulating laser cladding induced residual stresses with single and multiple clad beads. J Mater Process Technol 224:89–101
11. Farahmand P, Kovacevic R (2014) An experimental-numerical investigation of heat distribution and stress field in single- and multi-track laser cladding by a high-power direct diode laser. Opt Laser Technol 63:154–168
12. Gouge MF, Heigel JC, Michaleris P, Palmer TA (2015) Modeling forced convection in the thermal simulation of laser cladding processes. Int J Adv Manuf Technol 79(1):307–320
13. Nazemi N, Urbanic J (2017a) An experimental and simulation study for powder injection multi-track laser cladding of P420 stainless steel on AISI 1018 steel for selected mechanical properties. ASME J Manuf Sci Eng In press. https://doi.org/10.1115/1.4037604.
14. Nazemi N, Urbanic J, Alam M (2017b) Hardness and residual stress modeling of powder injection laser cladding of P420 coating on AISI 1018 substrate. Int J Adv Manuf Technol 93(1–19):3485–3503
15. Nazemi N, Alam M, Urbanic J, Saqib S, Edrisy A (2017c) A hardness study on laser cladded surfaces for a selected bead overlap conditions. SAE World Congress, Detroit
16. Nazemi N, Urbanic RJ, Saqib S (2017e) Utilizing a numerical simulation to model a step function response for 420 stainless steel powder laser cladding. ASME International Mechanical Engineering Congress and Exposition, November 3–9, Tampa, FL, USA
17. Heigel JC, Gouge MF, Michaleris P, Palmer TA (2016) Selection of powder or wire feedstock material for the laser cladding of Inconel. J Mater Process Technol 231:357–365
18. Zhao H, Zhang G, Yin Z, Wu L (2012) Three-dimensional finite element analysis of thermal stress in single-pass multi-layer weld-based rapid prototyping. J Mater Process Technol 212(1):276–285

19. Zhao H, Zhang G, Yin Z, Wu L (2011) A 3D dynamic analysis of thermal behavior during single-pass multi-layer weld-based rapid prototyping. J Mater Process Technol 211(3):488–495
20. Zhang CS, Li L, Deceuster A (2011) Thermomechanical analysis of multi-bead pulsed laser powder deposition of a nickel-based superalloy. J Mater Process Technol 211:1478–1487
21. Alimardani M, Toyserkani E, Huissoon J (2007) A 3D dynamic numerical approach for temperature and thermal stress distributions in multilayer laser solid freeform fabrication process. Opt Lasers Eng 45:1115–1130
22. Ding J, Colegrove P, Mehnen J, Williams S, Wang F, Almeida PS (2014) A computationally efficient finite element model of wire and arc additive manufacture. Int J Adv Manuf Technol 70(1–4):227–236
23. Ding J, Colegrove P, Mehnen J, Ganguly S, Almeida PMS, Wang F, Williams S (2011) Thermo-mechanical analysis of wire and arc additive layer manufacturing process on large multi-layer parts. Comput Mater Sci 50(12):3315–3322
24. Pu X, Zhang C, Li S, Deng D (2017) Simulating welding residual stress and deformation in a multi-pass butt-welded joint considering balance between computing time and prediction accuracy. Int J Adv Manuf Technol:1–12
25. Lei YW, Sun R, Tang Y, Niu W (2012) Numerical simulation of temperature distribution and TiC growth kinetics for high power laser clad TiC/NiCrBSiC composite coatings. Opt Laser Technol 44:1141–1147
26. Lie W, Ma J, Kong F, Liu S, Kovacenic R (2015) Numerical modeling and experimental verification of residual stress in autogenous laser welding of high-strength steel. Lasers Manuf Mater Process 2:24–42
27. Wang L, Felicelli S (2007) Process modeling in laser deposition of multilayer SS410 steel. J Manuf Sci Eng 129(6):1028–1034
28. Wen SY, Shin YC, Murthy JY, Sojka PE (2009) Modeling of coaxial powder flow for the laser direct deposition process. Int J Heat Mass Transf 52:5867–5877
29. Sowdari D, Majumdar P (2010) Finite element analysis of laser irradiated metal heating and melting process. Optics Laser Technol 42:855–865
30. Tabernero I, Lamikiz A, Ukar E, Lacalle LN, Angulo C, Urbikain G (2010) Numerical simulation and experimental validation of powder flux distribution in coaxial laser cladding. J Mater Process Technol 210(15):2125–2134

Publisher's Note